

Scanning Electron Thermal Absorbance Microscopy for Light Element Detection and Atomic Number Analysis

Ching-Che Lin, Shih-Ming Wang, Bo-Yi Chen, Cheng-Hung Chi, I-Ling Chang, and Chih-Wei Chang*

Cite This: *Nano Lett.* 2022, 22, 2667–2673

Read Online

ACCESS |

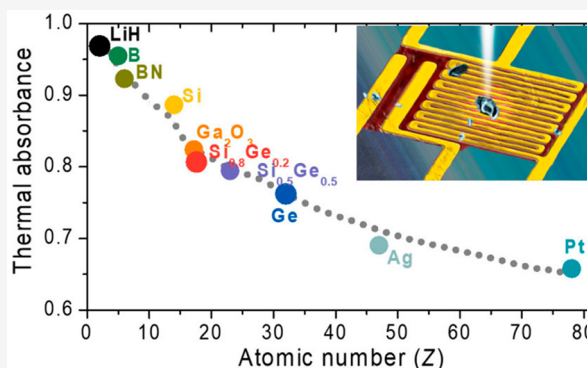
Metrics & More

Article Recommendations

Supporting Information

ABSTRACT: Recent developments in nanoscale thermal metrology using electron microscopy have made impressive advancements in measuring either phononic or thermal transport properties of nanoscale samples. However, its potential in material analysis has never been considered. Here we introduce a direct thermal absorbance measurement platform in scanning electron microscope (SEM) and demonstrate that its signal can be utilized for atomic number (Z) analysis at nanoscales. We prove that the measured absorbance of materials is complementary to signals of backscattering electrons but exhibits a much higher collection efficiency and signal-to-noise ratio. Thus, it not only enables successful detections of light elements/compounds under low acceleration voltages of SEM but also allows quantitative Z analyses in agreement with simulations. The direct thermal absorbance measurement platform would become an ideal tool for SEM, especially for thin films, light elements/compounds, or biological samples at nanoscales.

KEYWORDS: electron microscopy, thermal absorbance, atomic number, bolometer



We have recently witnessed rapid developments of nanoscale thermal metrology using electron microscopy; including detection of nanoscale temperature with $\sim 3\text{K}$ resolution,^{1–5} obtaining vibrational spectrum,^{6,7} and determining phonon-polariton dispersion curve.^{8,9} Adapting a scanning electron microscope (SEM) with a microthermometer has now become a quantitative heating source,¹⁰ facilitating measurements of thermal conductance across heterojunctions and interfaces with nanoscale spatial resolution.^{11–15} However, the physics probed by the nanoscale thermal metrology is always associated with either phonons or thermal transport properties. Material analyses have never been explored in the field of nanoscale thermal metrology.

Absorbance (A), which contains a lot of information on how a material absorbs the energy of incoming light/electron beam and converts it into varieties of excitations via dissipation processes, is a fundamental physical quantity of matters. The conservation of energy imposes that A must obey the following relation

$$A = 1 - R - T \quad (1)$$

which suggests that any reflectance (R) or transmittance (T) variations may have an opposite change in A . However, A is rarely directly measured but often indirectly obtained by separate measurements of R and T in eq 1. The experimental constrain would encounter many difficulties in nanoscale samples. First, dedicated calibration procedures are required to ensure eq 1 to hold in a measurement system. Second, the

optic apparatus such as an integrating sphere is not applicable in nanoscales because of the diffraction limit. Third, detectors designed for R and T have their own limitations and are usually not applicable to highly absorbing materials. Fourth, because of space constraints in electron microscopes, a significant part of R and T may be lost.

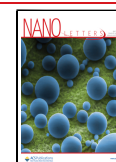
Because a significant portion of A usually converts into heat, here we introduce a thermal absorbance measurement platform that can directly measure the heat absorbed by the investigated sample.^{10,16} The platform can be adapted to various kinds of experimental setups. In this paper, we will focus on its applications in scanning electron microscopy (SEM) and exploit its analytical capabilities.

Since its invention in the 1930s and commercialization in the 1960s, the impact of SEM has been immense in diverse fields. By detecting secondary electrons (SE) or backscattered electrons (BSE), topographic and compositional contrast of samples can be resolved at nanoscales. However, SE or BSE detections in ordinary SEM are primarily for imaging purposes and do not exhibit quantitative analytical capabilities, which are

Received: November 22, 2021

Revised: March 6, 2022

Published: March 10, 2022



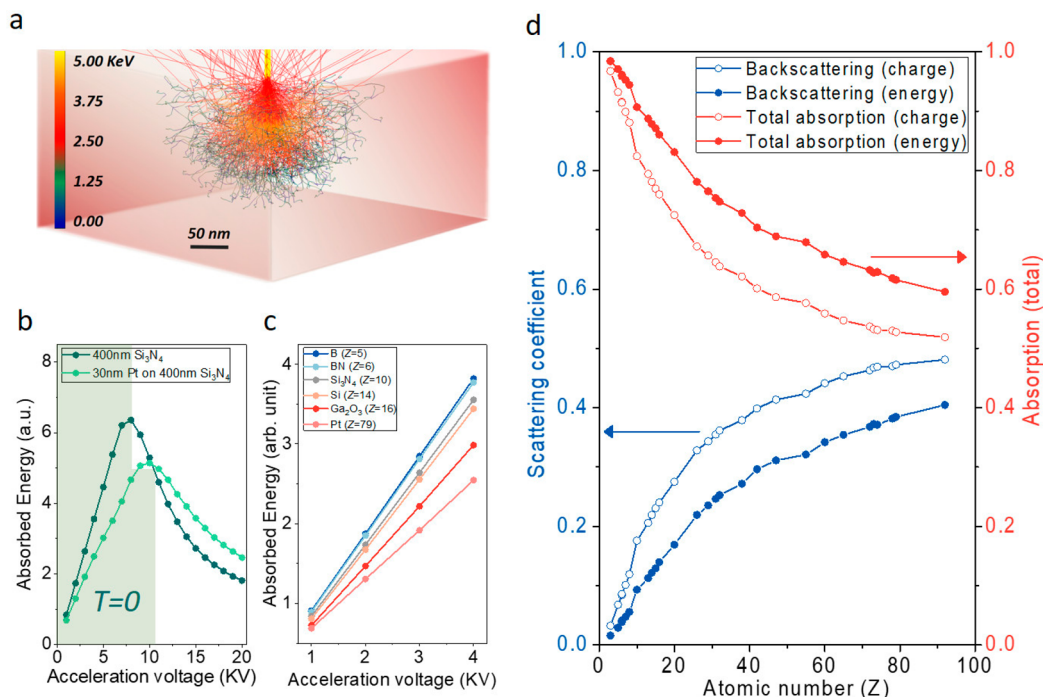


Figure 1. Simulated absorbance of an SEM beam interacting with a sample. (a) CASINO simulation of a 5 keV electron beam interacting with a 400 nm thick SiN_x , where the trajectories of the backscattered electrons (red) and absorbed electrons (green) are illustrated. (b) Simulated total absorbed energy vs V_{acc} for a 400 nm thick SiN_x film (dark green) and a 30 nm thick Pt film on the SiN_x film (green). The electrons would not penetrate the SiN_x film when $V_{\text{acc}} < 8$ kV, satisfying $T = 0$ condition (shaded area). (c) Simulated total absorbed energy vs V_{acc} for various materials when $T = 0$ is satisfied. (d) Simulated backscattered coefficient (blue symbols) and total absorbance coefficient (red symbols) vs atomic number (Z) of various samples when $T = 0$ is satisfied. The backscattered/absorbance coefficients for conservation of charge and energy are denoted by open and solid symbols, respectively.

the main drawback of SEM, and a lot of efforts have been devoted to overcoming them.^{17–21} Generally, the solutions are either attaching sophisticated energy analyzers to SEM or involving more dedicated calibration procedures.^{17–21}

Because BSE primarily contains elastic interactions between the incident beam and the sample, their signals, expressed as R in eq 1, are sensitive to the sample's atomic number (Z) and thus offer the potential for quantitative compositional analyses in SEM.²² However, because the interaction of the incident beam with the sample is much reduced for light elements/compounds, the corresponding BSE signals are weaker, and compositional analysis becomes difficult. The task becomes more challenging when low acceleration voltage ($V_{\text{acc}} < 5$ kV) and low current are required to reduce damage to light elements/compounds. Under low V_{acc} operation, sometimes a biased voltage needs to be applied to a BSE detector to filter out unwanted contributions from SEs, which complicates the calibration procedure.²³ Moreover, because the BSEs cover a wide range of angles, BSE detectors mounted at different locations would provide different image contrast at different V_{acc} 's, further reducing their ability for quantitative analysis.²⁴ Given that the detection of BSE is sensitively dependent on various parameters, the interpretation of its image contrast is not straightforward, and dedicated calibration is always required before performing quantitative analysis.

RESULTS

Monte Carlo Simulation. When a high-energy electron beam hits a sample, it will undergo a series of elastic/inelastic scatterings that eventually contribute to A , R , or T in eq 1. Figure 1a illustrates representative scattering processes of a V_{acc}

= 5 kV electron beam interacting with a 400 nm thick SiN_x using Monte Carlo simulation (CASINO package).^{25–27} The electrons scattered away from the sample at different angles respectively contribute to R and T in CASINO. However, those trapped inside the sample are regarded as A (Supporting Information S1). The CASINO program has been widely employed to describe backscattering or transmitted signals in SEM. Recently quantitative comparisons have been made to understand A via thermal absorbance measurements of SiN_x films as well.¹⁰ Figure 1b shows simulated A vs V_{acc} for the 400 nm thick SiN_x film. We find that A increases nearly linearly with V_{acc} and reaches a peak when $V_{\text{acc}} = V_p$. The V_p is the threshold voltage beyond which some electrons would transmit through the specimen, and $T = 0$ no longer holds.

From the CASINO simulation, we find V_p is sensitively dependent on the atomic number (Z) and sample thickness. When the sample is thick enough, or V_{acc} is sufficiently low, $T = 0$ and thus $A + R = 1$. Under the condition, A is linearly dependent on V_{acc} , and the slope is larger for light elements, as shown in Figure 1c. In general, A and R are complementary and display opposite dependencies on Z , as displayed in Figure 1d. Thus, it is advantageous to detect light elements via measuring A . Furthermore, while eq 1 respectively holds for the conservation of charge and conservation of energy, in practice a BSE detector detects electrical currents but the absorbance is often measured by energy fluxes. The subtle difference makes the contribution of A higher than $1 - R$ naively estimated from the BSE electrical current signal. For example, as shown in Figure 1d, the conservation of energy demands that 91% of the incident electron beam energy is absorbed by a $Z = 10$ material, whereas conservation of charge indicates that

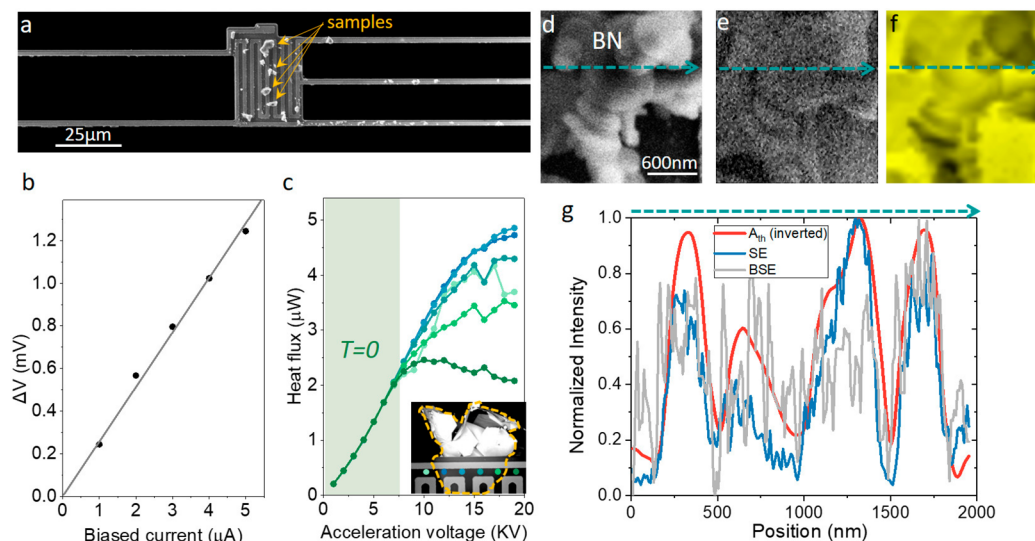


Figure 2. Device characterizations and measurements. (a) SEM image of the direct thermal absorbance measurement platform with investigated samples (denoted by the arrows) deposited on it. (b) Signal vs biased current when irradiating a 400 nm thick SiN_x film by a 5 keV electron beam. (c) Measured heat flux (P_{th}) vs V_{acc} for different positions of a SiN_x . In this device, although some materials (enclosed by the yellow dashed line in the inset) are unintentionally attached beneath the suspended SiN_x , all results still converge into a single curve when $V_{\text{acc}} < 7$ kV, indicating $T = 0$ is satisfied (denoted by the shaded area). The positions of the electron beam are respectively labeled in accordance with the symbols in the figure. (d–f) SE, BSE, and P_{th} images of a BN powder. (g) The corresponding line profile selected from the dashed line. The signals of P_{th} have been inverted in (g) to compare with those of SE and BSE.

82% of the incident electrons are trapped in the material. Moreover, Figure 1d suggests that the change of A or R is $1.3\%/\Delta Z$ for $Z < 30$ and $0.2\%/\Delta Z$ for $Z > 30$; thus, the system must have sufficiently high S/N to distinguish unitary Z variations. BSE detectors, because of their poor detection efficiency, large electronic noise, and weak responses to light elements, usually have $S/N < 40$ and cannot meet our purpose.¹⁹

The absorbance A contains various forms of excitations, including emissions of SEs (A_{SE}), cathodoluminescence (A_{CL}), electron beam induced currents (A_{EBIC}), X-rays ($A_{\text{X-ray}}$), thermal energy (A_{th}), and so on, obeying

$$A = A_{\text{SE}} + A_{\text{CL}} + A_{\text{EBIC}} + A_{\text{X-ray}} + A_{\text{th}} + \dots \quad (2)$$

In principle, it is not guaranteed that any of the above excitations would be complementary to R . We have known that A_{SE} is sensitive to surface morphology and its relation to Z is indirect and complex.¹⁷ Signals of A_{CL} are always weak and are sensitive to material bandgap rather than Z . Because of its poor S/N, the capability of using A_{CL} for material analysis is limited.²⁸ A_{EBIC} is sensitive to bandgap or junctions of semiconductors and has never been shown to be Z sensitive. Analyzing $A_{\text{X-ray}}$ is the basis of electron probe microanalysis (EPMA), but it usually operates under high V_{acc} and high beam currents.^{29,30} The unavoidable background contribution would limit its capability in analyzing thin samples. Besides, EPMA equipped with wavelength dispersive X-ray spectroscopy (WDS) need to add different channels of analyzers that are expensive and incompatible with ordinary SEM. Our last choice is to measure A_{th} . To demonstrate that A_{th} can be used as a probe for material analysis, one must show that it is complementary to BSE signals and exhibits a sufficiently high S/N. This is the primary motivation of our work.

Features of Thermal Absorbance Measurements. Like bolometers, we fabricated direct thermal absorbance platforms consisting of a suspended SiN_x pad with patterned Pt

resistance thermometers on it (Supporting Information S2). As shown in Figure 2a, investigated samples were deposited on the pad, and its heat current (P_{th}) was directly measured by positioning the electron beam of SEM on the sample and monitoring the temperature rise of the pad via four-probe resistance measurement. Similar platforms had been employed in our previous thermal conductivity measurements of nanowires.^{12,31,32}

Figure 2b shows that when irradiating a 400 nm thick SiN_x with a focused electron beam under $V_{\text{acc}} = 5$ kV and beam current 309 pA, the voltage response of the platform is linearly proportional to I_{DC} with zero offsets, demonstrating that the signal is thermal in nature. From the data, we obtain $P_{\text{th}} = 0.719 \mu\text{W}$ and $A_{\text{th}} = P_{\text{th}}/P_{\text{ebeam}} = 89\%$ (where $P_{\text{ebeam}} = V_{\text{acc}} \times$ beam current). If assuming $x = 1.33$ for the SiN_x film and comparing it with the A obtained from the CASINO simulation, we obtain $A_{\text{th}}/A = 98\%$. Thus, a majority of the absorbed energy is converted into heat, and it agrees with the previous result by Yuan et al.¹⁰ We have also demonstrated that S/N exceeds 4000 (Supporting Information S3), much higher than that of typical BSE detectors.

The better S/N can be attributed to three aspects. First, A is generally higher than 70%, but R is always less than 30% for $Z < 50$, as shown in Figure 1d. Second, P_{th} is proportional to P_{ebeam} , whereas a BSE detector detects the electron beam current instead. So P_{th} is further gained by V_{acc} . Third, because thermal radiation is negligible, all P_{th} generated by the sample is collected by the platform with almost 100% detection efficiency. The nearly 100 times improvement of S/N of the platform over that of typical BSE detectors would enable sensitive detections of light elements/compounds and precise compositional analysis.

Figure 2c displays P_{th} vs V_{acc} of SiN_x at different locations of our platform, in which some materials are unintentionally attached beneath it, as shown in the inset. Interestingly, we find that even though the unwanted materials can affect P_{th} when

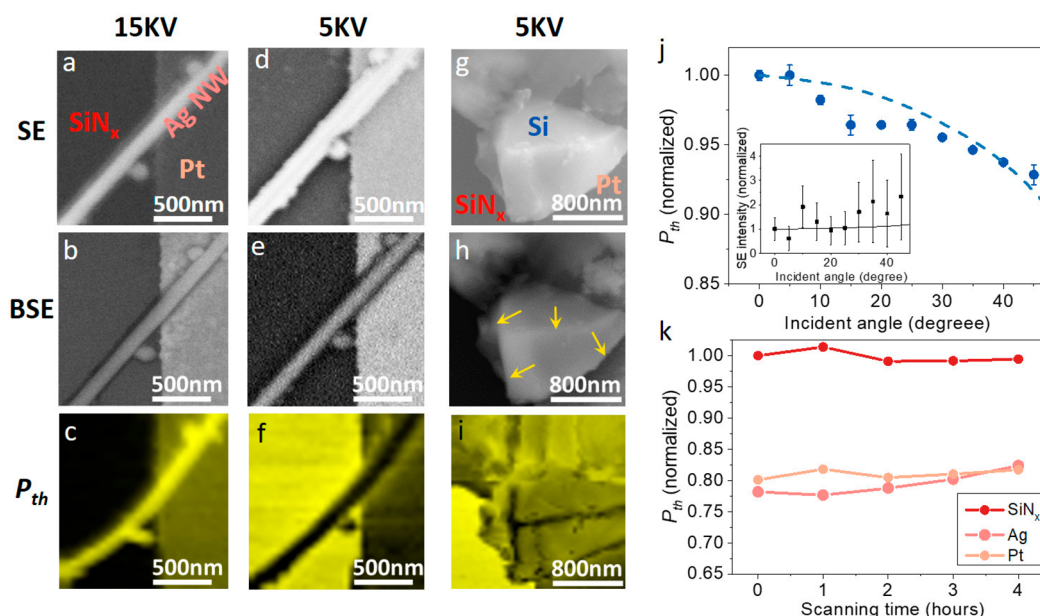


Figure 3. General features of SE, BSE, and P_{th} mapping. (a–f) Here an Ag nanowire (AgNW) deposited on the platform is respectively imaged under $V_{acc} = 15$ kV (a–c) and $V_{acc} = 5$ kV (d–f) using SE (a,d), BSE (b,e), and P_{th} (c,f) detectors. (g–i) SE, BSE, and P_{th} image of a Si crystal with edges (denoted by the yellow arrows in h). (j) Normalized P_{th} vs incident angle of the electron beam on the surface. Here, the electron beam spot positioned at “Si” labeled in (g) is used for analysis. The incident angle is the angle between the incident electron beam and the normal vector at “Si”. The corresponding SE signal vs incident angle is shown in the inset. The SE signals are normalized to their initial value at zero degree. (k) Normalized P_{th} of SiN_x (red), AgNW (dark pink), and Pt (light pink) during prolonged scanning time that hydrocarbon deposition occurs.

$V_{acc} > 8$ kV, they merge into a single line for $V_{acc} < 7$ kV. Because Figure 1b has suggested that electrons cannot penetrate the SiN_x for $V_{acc} < 7$ kV, Figure 2c demonstrates that A_{th} can be uniquely determined once $T = 0$ is satisfied.

In addition, P_{th} mapping can be carried out by mounting the platform on a piezo-scanner and using the spot function of SEM to enable raster scans. Given our piezo-scanner’s limited fine motion scanning range, current P_{th} images are usually less than $2.3 \mu m \times 2.3 \mu m$ with spatial resolution being limited by the interaction volume and the spot size of the electron beam (Supporting Information S4 and S5). The corresponding SE or BSE images are also acquired for comparison. Figure 2d–f shows the SE, BSE, and P_{th} images of a BN powder. The images and line profiles have been normalized for comparison. Because of the weak BSE signals, we have applied a median filter to reduce its noise. A representative line profile of the images (here, the contrast of P_{th} has been normalized and inverted to compare with those of SE and BSE) is drawn in Figure 2g. We see that P_{th} is complementary to both SE or BSE but exhibits much-reduced noise.

We next survey some general features of P_{th} . Figure 3a–c shows SE, BSE, and P_{th} images of an Ag nanowire mapped under $V_{acc} = 15$ kV. The diameter of the Ag nanowire is 140 nm. Here the P_{th} image is found to show similar contrast to SE and BSE images; that is, the Ag nanowire and the Pt film appear to be brighter than the SiN_x . Interestingly, when V_{acc} is reduced to 5 kV, the contrast between P_{th} and SE or BSE images is reversed, as shown in Figure 3d–f. The observation can be understood as follows. Under 15 kV, the SEM electron beam can penetrate the Ag nanowire and the underneath platform made by Pt/ SiN_x ; thus, the detected P_{th} is the total thermal energy absorbed by the Ag nanowire and Pt/ SiN_x . Thus, the P_{th} signals decrease from $P_{th}(Ag+Pt+SiN_x)$, $P_{th}(Pt+SiN_x)$, and $P_{th}(SiN_x)$ under $V_{acc} = 15$ kV. However, because the electron beam cannot penetrate these samples at $V_{acc} = 5$

kV, the P_{th} image shows the opposite contrast to the BSE image.

Edges and tilted facets are known to enhance overall SE and BSE signals, and it would be interesting to investigate the corresponding P_{th} variations.³³ Figure 3g–i shows the SE, BSE, and P_{th} image of a Si crystal. Notably, while the edges appear brighter in SE and BSE images, they are darker in the P_{th} image. The result again confirms that P_{th} is complementary to SE or BSE signals. Furthermore, when increasing the incident angle of the electron beam, we find P_{th} of the facet decreases and displays less than 2% deviation from the CASINO simulation, as shown in Figure 3j. However, as shown in the inset of Figure 3j, the poor S/N and the limited solid angle of the SE detector make it difficult to collect all electrons and the corresponding effect of tilting in SE, as well as in BSE,³⁴ is hard to analyze quantitatively.

Hydrocarbon deposition is a common problem for low-voltage SEM. Figure 3k displays P_{th} of an Ag nanowire, SiN_x , and Pt under prolonged electron beam radiation. Curiously, while hydrocarbon deposition is visible in SE images, it is too thin to stop the penetration of the 5 keV electron beam. Thus, the measured P_{th} ’s are still dominated by the underneath SiN_x and Pt samples. However, we find that P_{th} increases by 6% in the Ag nanowire. We speculate that its geometry could induce more hydrocarbon deposition, so the change in P_{th} is more pronounced.

Dependence on Atomic Number. So far, SE and BSE images have shown similar trends of contrast variations, and it is not easy to distinguish their respective correlation with P_{th} . However, we have known that BSE signals are sensitive to the atomic number (Z) of elements or averaged atomic number (Z_{ave}) of compounds, whereas SE signals do not exhibit similar characteristics.¹⁹ Thus, surveying the dependencies of A_{th} on Z or Z_{ave} will reveal A_{th} ’s respective relation to SE or BSE. To minimize location variations of P_{th} on the platform, the P_{th} of

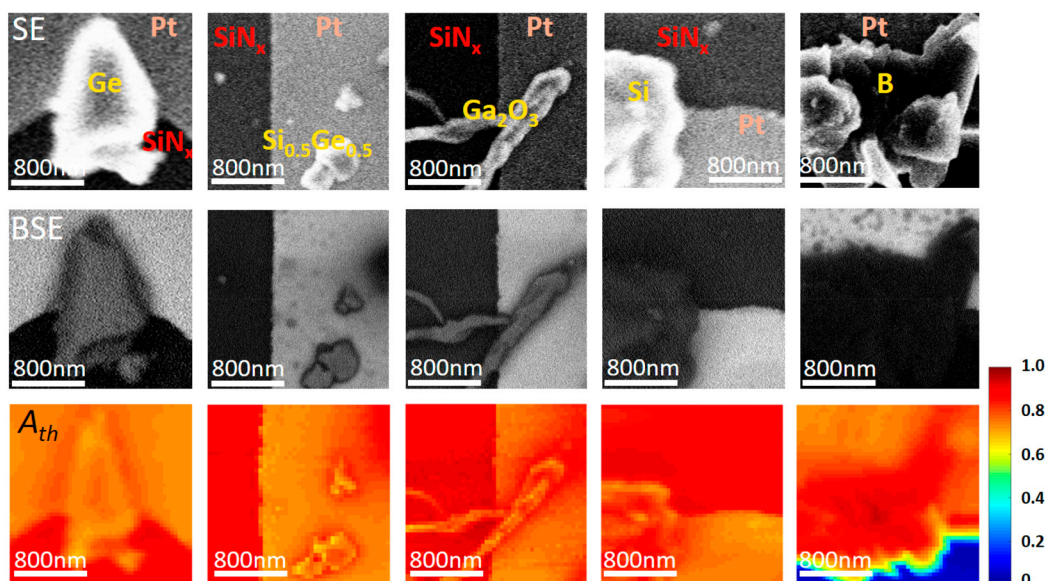


Figure 4. SE (first row), BSE (second row), and A_{th} (third row) images. The images are taken under $V_{acc} = 5$ kV for the investigated materials (denoted by the labels) deposited on the platform. Here the contrast of BSE images is kept the same during imaging, but that of SE is adjusted from sample to sample to yield better image quality. Note that while the brightness and contrast of SE or BSE images can be arbitrarily changed depending on the SEM settings, both of them are absolute in A_{th} images, representing the thermal absorbance of materials.

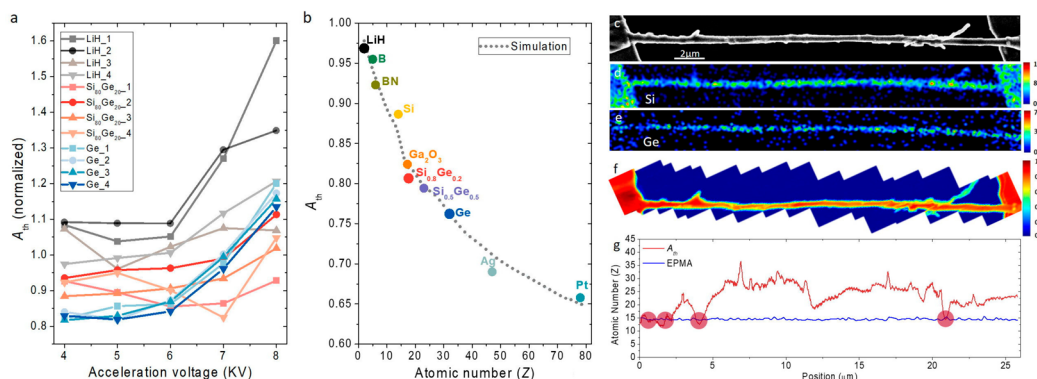


Figure 5. A_{th} of the investigated materials and Z of a $Si_{1-x}Ge_x$ nanowire determined by A_{th} and EPMA. (a) A_{th} vs V_{acc} of randomly selected spots of the investigated materials. Deviations within the same materials are found because of effects from edges, tilted facets, thin samples, hydrocarbon depositions, and so on. Here A_{th} 's are normalized to that of SiN_x . (b) A_{th} vs atomic number (Z) of the investigated materials under $V_{acc} = 5$ kV when the strongest A_{th} is chosen as a representative signal free from the unwanted perturbations. A obtained from CASINO simulation (dotted curve) is drawn for comparison. (c) SEM image of a polycrystalline $Si_{1-x}Ge_x$ nanowire suspended across the measurement platform. (d,e) X-ray intensity mapping of Si (d) and Ge (e) obtained by EPMA under $V_{acc} = 10$ kV. (f) A_{th} mapping under $V_{acc} = 5$ kV. (g) Z variations along the nanowire, respectively determined by A_{th} (red line) and EPMA (blue line). The red circles denote the strongest A_{th} 's measured in the nanowire.

an investigated sample is normalized by that of a nearby SiN_x to obtain its $A_{th,sample}$ via $A_{th,sample} = P_{th,sample}/P_{ebeam} = 0.89(P_{th,sample}/P_{th,SiN_x})$.

Figure 4 displays representative SE, BSE, and A_{th} images of grains of Pt ($Z = 78$), Ge ($Z = 32$), $Si_{0.5}Ge_{0.5}$ ($Z_{ave} = 23$), Ga_2O_3 ($Z = 17.2$), Si ($Z = 14$), and B ($Z = 5$) under $V_{acc} = 5$ kV. Because of our direct measurement of A_{th} , the brightness and contrast shown in Figure 4 can be directly interpreted as the map of thermal absorbance, which are physical quantities rather than those in SE or BSE images that can be arbitrarily changed by the instrumental settings. Furthermore, the signals of A_{th} and BSE show opposite trends when imaging materials with low Z , whereas SE images do not display a similar effect. We also find that, unlike SE, A_{th} is less sensitive to topographic features, especially when imaging the B powder.

Figure 5a shows representative normalized A_{th} vs V_{acc} for randomly chosen spots from a given material. To compare A_{th}

signals from different platforms, we have normalized their signals to those of SiN_x . Most A_{th} 's appear to be independent of V_{acc} when $V_{acc} < 6$ kV, indicating that the electron beam would not penetrate the sample and $T = 0$ is satisfied. However, we also find some undesired deviations in LiH or $Si_{0.8}Ge_{0.2}$, which could inhibit further analyses.

We have learned that edges or tilted facets would reduce the signal of A_{th} ; transmitted electrons or hydrocarbon deposition could cause signal variations of A_{th} as well. In addition, signals could take longer to stabilize, especially when employing $V_{acc} < 5$ kV for mapping (Supporting Information S4). Thus, the electron beam must be incident normally on a sample surface free from edges or tilted facets to implement the quantitative analysis. It must be free from hydrocarbon contamination and satisfy the $T = 0$ condition, too. Experimentally, we can reduce carbon contamination by decreasing the acquisition time. A sufficiently high V_{acc} can be chosen so that most electrons can

penetrate the thin hydrocarbon layer. But V_{acc} must also be low enough to ensure $T = 0$. Empirically, we find that $V_{\text{acc}} = 5$ kV suits our purpose. Additionally, the brightest spot within a given sample is chosen as the representative A_{th} signal to avoid effects from thin samples, signal instabilities, edges, or tilted facets.

Following the guideline, Figure 5b shows A_{th} vs Z under $V_{\text{acc}} = 5$ kV. The simulated A vs Z shown in Figure 1d is also drawn for comparison. Even though eq 2 has suggested that A_{th} is a subset of A , Figure 5b demonstrates that the measured A_{th} vs Z generally follows the simulated A vs Z with less than 2% deviation. The result independently confirms the $A_{\text{th}}/A > 98\%$ established in Figure 2(b and c) for the SiN_x film.¹⁰ For A_{th} 's of $\text{Si}_{1-x}\text{Ge}_x$ alloys, including Si ($Z = 14$), $\text{Si}_{0.8}\text{Ge}_{0.2}$ ($Z_{\text{ave}} = 17.6$), $\text{Si}_{0.5}\text{Ge}_{0.5}$ ($Z_{\text{ave}} = 23$), and Ge ($Z = 32$), Figure 5b suggests that a 10% uncertainty in estimating x can be reached if using the CASINO simulation as a calibration curve.

DISCUSSION

Compared with other competing techniques, quantitative compositional analyses based on BSE detectors have recently been conducted in $\text{In}_x\text{Ga}_{1-x}\text{As}$ ($Z_{\text{ave}} = 65.8\text{--}71.2$ for $x = 0.1\text{--}0.4$) layers with 10% accuracy, but it is reached only when using $V_{\text{acc}} = 25$ kV.¹⁸ A dedicated calibration procedure is proposed to analyze the contrast of BSE images of GaAs/AlAs and $\text{Al}_{0.22}\text{Ga}_{0.78}\text{N}/\text{GaN}$ layers.¹⁹ But the Z -dependent BSE calibration curve displays unexpected jumps or dips that would cause Z estimation highly uncertain.¹⁹ We also contest our capability with EPMA in determining Z of a $\text{Si}_{1-x}\text{Ge}_x$ nanowire shown in Figure 5c. Because ordinary EPMA generally operates at $V_{\text{acc}} = 10$ kV or higher, its electron beam would penetrate the investigated sample and the background contributions would make the compositional analysis incorrect, we have thus suspended the nanowire and made sure that the background signals are free from Si or Ge, as shown in Figure 5d,e. EPMA determines x to be 0.01–0.09, corresponding to $Z = 14.18\text{--}15.62$. However, as shown in Figure 5f,g, the polycrystalline nature of the nanowire makes its surface full of edges and tilted facets, so A_{th} signals are generally lower than expected and display large fluctuations. Nevertheless, if the strongest A_{th} is selected, the Z determined from both techniques is consistent. Considering its flexibilities and much-reduced cost, our direct A_{th} measurements platform would be ideally suited for preliminary analyses of semiconductors or characterizing organic or biological samples whose X-ray are too weak to be detected by EPMA.

ASSOCIATED CONTENT

Supporting Information

The Supporting Information is available free of charge at <https://pubs.acs.org/doi/10.1021/acs.nanolett.1c04502>.

Details of CASINO simulation, device fabrication, measurement calibration, experimental mapping methods, characterizations of spatial resolution (PDF)

AUTHOR INFORMATION

Corresponding Author

Chih-Wei Chang – Center for Condensed Matter Sciences, National Taiwan University, Taipei 10617, Taiwan; Center of Atomic Initiative for New Materials (AI-MAT), National Taiwan University, Taipei 10617, Taiwan; orcid.org/0000-0003-0956-3179; Email: cwchang137@ntu.edu.tw

Authors

Ching-Che Lin – Center for Condensed Matter Sciences, National Taiwan University, Taipei 10617, Taiwan

Shih-Ming Wang – Center for Condensed Matter Sciences, National Taiwan University, Taipei 10617, Taiwan; Department of Mechanical Engineering, National Cheng Kung University, Tainan 70101, Taiwan

Bo-Yi Chen – Center for Condensed Matter Sciences, National Taiwan University, Taipei 10617, Taiwan

Cheng-Hung Chi – Center for Condensed Matter Sciences, National Taiwan University, Taipei 10617, Taiwan

I-Ling Chang – Department of Mechanical Engineering, National Cheng Kung University, Tainan 70101, Taiwan

Complete contact information is available at:

<https://pubs.acs.org/10.1021/acs.nanolett.1c04502>

Notes

The authors declare no competing financial interest.

ACKNOWLEDGMENTS

This work is supported by Ministry of Science and Technology of Taiwan (MOST 110-2112-M-002-008 and 110-2119-M-002-010-MBK), and Center of Atomic Initiative for New Materials, National Taiwan University, from the Featured Areas Research Center Program within the framework of the Higher Education Sprout Project by the Ministry of Education in Taiwan (108L9008).

REFERENCES

- Mecklenburg, M.; et al. Nanoscale temperature mapping in operating microelectronic devices. *Science* **2015**, *347*, 629–632.
- Idrobo, J. C.; et al. Temperature Measurement by a Nanoscale Electron Probe Using Energy Gain and Loss Spectroscopy. *Phys. Rev. Lett.* **2018**, *120*, 095901.
- Lagos, M. J.; Batson, P. E. Thermometry with Subnanometer Resolution in the Electron Microscope Using the Principle of Detailed Balancing. *Nano Lett.* **2018**, *18*, 4556–4563.
- Mecklenburg, M.; Zutter, B.; Regan, B. C. Thermometry of Silicon Nanoparticles. *Phys. Rev. Appl.* **2018**, *9*, 014005.
- Shen, L.; Mecklenburg, M.; Dhall, R.; Regan, B. C.; Cronin, S. B. Measuring nanoscale thermal gradients in suspended MoS₂ with STEM-EELS. *Appl. Phys. Lett.* **2019**, *115*, 153108.
- Krivanek, O. L.; et al. Vibrational spectroscopy in the electron microscope. *Nature* **2014**, *514*, 209.
- Rez, P.; Aoki, T.; March, K.; Gur, D.; Krivanek, O. L.; Dellby, N.; Lovejoy, T. C.; Wolf, S. G.; Cohen, H. Damage-free vibrational spectroscopy of biological materials in the electron microscope. *Nat. Commun.* **2016**, *7*, 10945.
- Li, N.; Guo, X.; Yang, X.; Qi, R.; Qiao, T.; Li, Y.; Shi, R.; Li, Y.; Liu, K.; Xu, Z.; Liu, L.; Garcia de Abajo, F. J.; Dai, Q.; Wang, E.-G.; Gao, P. Direct observation of highly confined phonon polaritons in suspended monolayer hexagonal boron nitride. *Nat. Mater.* **2021**, *20*, 43–48.
- Qi, R.; Shi, R.; Li, Y.; Sun, Y.; Wu, M.; Li, N.; Du, J.; Liu, K.; Chen, C.; Chen, J.; Wang, F.; Yu, D.; Wang, E.-G.; Gao, P. Measuring phonon dispersion at an interface. *Nature* **2021**, *599*, 399–403.
- Yuan, P.; Wu, J. Y.; Ogletree, D. F.; Urban, J. J.; Dames, C.; Ma, Y. Adapting the Electron Beam from SEM as a Quantitative Heating Source for Nanoscale Thermal Metrology. *Nano Lett.* **2020**, *20*, 3019–3029.
- Liu, D.; Xie, R. G.; Yang, N.; Li, B. W.; Thong, J. T. L. Profiling Nanowire Thermal Resistance with a Spatial Resolution of Nanometers. *Nano Lett.* **2014**, *14*, 806–812.
- Hsiao, T. K.; et al. Micron-scale ballistic thermal conduction and suppressed thermal conductivity in heterogeneously-interfaced nanowires. *Phys. Rev. B* **2015**, *91*, 035406.

- (13) Lee, S. Y.; Lee, W. Y.; Thong, J. T. L.; Kim, G. S.; Lee, S. K. Lateral heat flow distribution and defect-dependent thermal resistance in an individual silicon nanowire. *Nanotechnology* **2016**, *27*, 115402.
- (14) Zhao, X.; Xu, L.; Sun, M.; Ma, W.; Wu, X.; Xu, C.; Kuang, H. Engineering the thermal conductivity along an individual silicon nanowire by selective helium ion irradiation. *Nat. Commun.* **2017**, *8*, 15919.
- (15) Zhao, Z.; Zhang, J.-W.; Lu, S.-H.; Zhang, H.; Liu, F.; Fu, B.; Zhao, M.-Q.; Liu, H. Probing thermal transport across amorphous region embedded in a single crystalline silicon nanowire. *Sci. Rep.* **2020**, *10*, 821.
- (16) Swinkels, M. Y.; et al. Measuring the Optical Absorption of Single Nanowires. *Phys. Rev. Appl.* **2020**, *14*, 024045.
- (17) El-Gomati, M. M.; Walker, C. G. H.; Zha, X. Towards quantitative scanning electron microscopy: Applications to nano-scale analysis. *Nucl. Instrum. Meth. A* **2011**, *645*, 68–73.
- (18) Muller, E.; Gerthsen, D. Composition quantification of electron-transparent samples by backscattered electron imaging in scanning electron microscopy. *Ultramicroscopy* **2017**, *173*, 71–75.
- (19) Garitagaitia Cid, A.; Rosenkranz, R.; Löffler, M.; Clausner, A.; Standke, Y.; Zschech, E. Quantitative analysis of backscattered electron (BSE) contrast using low voltage scanning electron microscopy (LVSEM) and its application to Al_{0.22}Ga_{0.78}N/GaN layers. *Ultramicroscopy* **2018**, *195*, 47–52.
- (20) Han, W.; Zheng, M.; Banerjee, A.; Luo, Y. Z.; Shen, L.; Khursheed, A. Quantitative material analysis using secondary electron energy spectromicroscopy. *Sci. Rep.* **2020**, *10*, 22144.
- (21) Skoupy, R.; Fort, T.; Krzyzaneck, V. Nanoscale Estimation of Coating Thickness on Substrates via Standardless BSE Detector Calibration. *Nanomaterials* **2020**, *10*, 332.
- (22) Kanaya, K.; Okayama, S. Penetration and Energy-Loss Theory of Electrons in Solid Targets. *J. Phys. D: Appl. Phys.* **1972**, *5*, 43.
- (23) Cid, A. G.; Sedighi, M.; Löffler, M.; van Dorp, W. F.; Zschech, E. Energy-Filtered Backscattered Imaging Using Low-Voltage Scanning Electron Microscopy: Characterizing Blends of ZnPc-C-60 for Organic Solar Cells. *Adv. Eng. Mater.* **2016**, *18*, 913–917.
- (24) Wright, S. I.; Nowell, M. M.; de Kloe, R.; Camus, P.; Rampton, T. Electron imaging with an EBSD detector. *Ultramicroscopy* **2015**, *148*, 132–145.
- (25) Hovington, P.; Drouin, D.; Gauvin, R. CASINO: A new Monte Carlo code in C language for electron beam interaction.1. Description of the program. *Scanning* **1997**, *19*, 1–14.
- (26) Hovington, P.; Drouin, D.; Gauvin, R.; Joy, D. C.; Evans, N. CASINO: A new Monte Carlo code in C language for electron beam interactions.3. Stopping power at low energies. *Scanning* **1997**, *19*, 29–35.
- (27) Drouin, D.; Hovington, P.; Gauvin, R. CASINO: A new Monte Carlo code in C language for electron beam interactions.2. Tabulated values of the Mott cross section. *Scanning* **1997**, *19*, 20–28.
- (28) Masuda, Y.; Kamiya, M.; Sugita, A.; Inami, W.; Kawata, Y.; Kominami, H.; Nakanishi, Y. Spatial resolution and cathodoluminescence intensity dependence on acceleration voltage in electron beam excitation assisted optical microscopy using Y₂O₃:Eu³⁺ film. *Ultramicroscopy* **2017**, *182*, 212–215.
- (29) Llovet, X.; Moy, A.; Pinard, P. T.; Fournelle, J. H. Electron probe microanalysis: A review of recent developments and applications in materials science and engineering. *Prog. Mater. Sci.* **2021**, *116*, 100673.
- (30) Rinaldi, R.; Llovet, X. Electron Probe Microanalysis: A Review of the Past, Present, and Future. *Microsc. Microanal.* **2015**, *21*, 1053–1069.
- (31) Wingert, M. C.; Chen, Z. C. Y.; Kwon, S.; Xiang, J.; Chen, R. K. Ultra-sensitive thermal conductance measurement of one-dimensional nanostructures enhanced by differential bridge. *Rev. Sci. Instrum.* **2012**, *83*, 024901.
- (32) Hsiao, T.-K.; Chang, H.-K.; Liou, S.-C.; Chu, M.-W.; Lee, S.-C.; Chang, C.-W. Observation of room temperature ballistic thermal conduction persisting over 8.3 micrometers in SiGe nanowires. *Nat. Nanotechnol.* **2013**, *8*, 534–538.
- (33) Reimer, L.; Riepenhausen, M.; Schierjott, M. Signal of Backscattered Electrons at Edges and Surface Steps in Dependence on Surface Tilt and Take-Off Direction. *Scanning* **1986**, *8*, 164–175.
- (34) Hejna, J. Topographic and material contrast in low-voltage scanning electron microscopy. *Scanning* **1995**, *17*, 387–394.

Supporting Information

Scanning electron thermal absorbance microscopy for light element detection and atomic number analysis

Ching-Che Lin,¹ Shih-Ming Wang,^{1,2} Bo-Yi Chen,¹ Cheng-Hung Chi,¹ I-Ling Chang,² and Chih-Wei Chang^{1,3*}

¹ Center for Condensed Matter Sciences, National Taiwan University, Taipei 10617, Taiwan

² Department of Mechanical Engineering, National Cheng Kung University, Tainan 70101, Taiwan

³ Center of Atomic Initiative for New Materials (AI-MAT), National Taiwan University, Taipei, 10617, Taiwan

S1. Details of CASINO Simulation

To simulate the interaction of incident electrons with a sample, we employ the CASINO Monte Carlo program (Version 3.3.0.4)^[1] to characterize the interaction volume, reflectance (R), transmittance (T), and total absorbance (A).

The simulations are performed with the default physical models (MONSEL Defaults), which means the calculation of Mott elastic scattering cross-section is modeled by Browning^[2], and inelastic scattering energy loss (dE/dS) calculation is modeled by Joy and Luo^[3] and further modified by Lowney^[4]. We input 100,000 electrons with an electron beam diameter 10 nm under various acceleration voltages V_{acc} (1-20 KV). Sample's density and composition are obtained from the database of CASINO.

As an example, Fig. S1(a) presents the simulated backscattering and transmitted coefficients of Si_3N_4 as a function of V_{acc} . Here we set the size of a square Si_3N_4 to be 5 μm in length and 400 nm in thickness. Si_3N_4 's atomic number (Z) is 10, and its density is 3.17 g/cm³. The backscattered or transmitted coefficients are obtained by counting the number of electrons in the backscattered/transmitted trajectories and normalize them by the number of incident electrons.

The CASINO simulation can also obtain the energy distribution of transmitted and backscattered electrons. When an incident 10KeV electron beam interacts with the 400nm thick Si_3N_4 film, the energy distributions of transmitted and backscattered electrons are shown in Fig. S1(b & c). The energy of backscattered/transmitted

electrons are obtained by integrating the two distributions, as shown in Fig. S1(d). Similarly, the absorbed energy and absorbance can be obtained, as shown in Fig. S1(e,f).

As shown in Fig. S1(e,f), we find the absorbed energy increases linearly with V_{acc} in the $V_{acc} < 6\text{KV}$ range. Different elements or compounds have different slopes when $T=0$ is satisfied. The slopes are sensitively dependent on the atomic number of the element/compound, which constitutes the basis for quantitative composition from CASINO simulation.

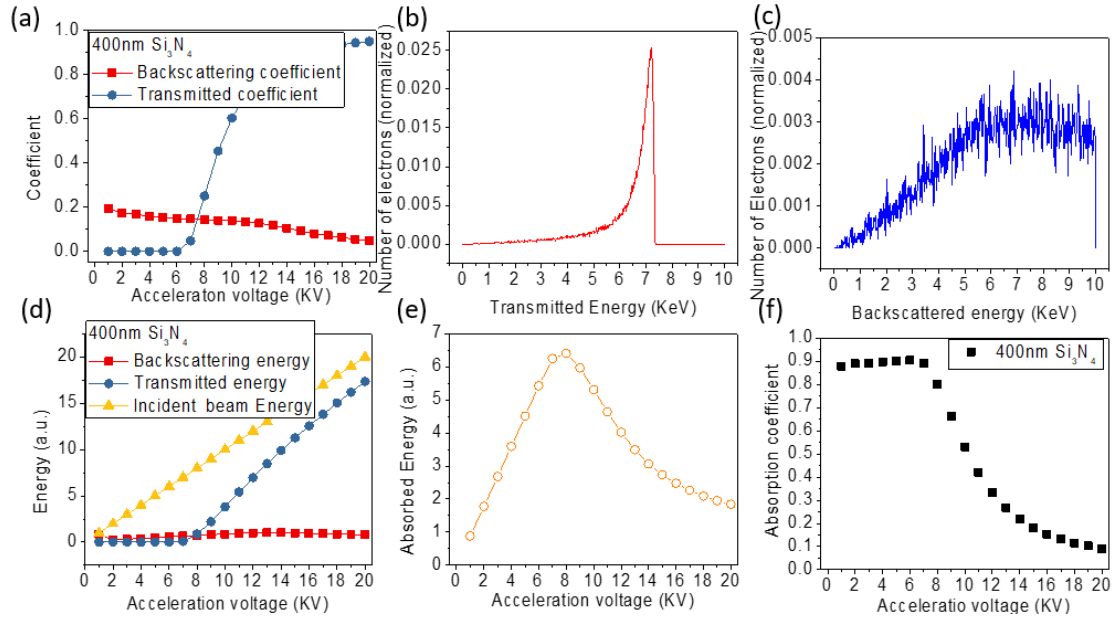


Fig. S1. CASINO Monte Carlo simulation of the interaction between incident beam electrons and 400 nm thick Si_3N_4 film. (a) backscattering coefficient and transmitted coefficient as a function of beam energy. (b & c) Transmitted (b) and backscattered (c) energy distribution spectrum under $V_{acc}=10\text{KV}$. Here the number of transmitted /backscattered electrons are normalized to that of the incident electrons. (d) Backscattered energy (red), transmitted energy (blue), and incident energy (yellow) vs. V_{acc} . (e) Total absorbed energy vs. V_{acc} . (f) Absorbance vs. V_{acc} .

S2. Device fabrication

The device fabrication procedure is shown in Fig. S2. Prior to the fabrication process, the Si wafer were subjected to a standard RCA cleaning procedure and subsequently, a 400 nm thick optimized low-stress Si-rich LPCVD SiN_x layer was deposited to serve as a support material in which thin Cr/Pt metallic film are suspended. Before lithography process begin, substrates were put in the oven at 125°C for 30mins as dehydration bake. A positive photoresist (S1813, Shipley Inc.) was further spin-coated on substrates at 4000 rpm for 45 s, and soft-baked at 120°C for 1.5 min. The full 4-inch wafer is then exposed for 20 seconds in a hard-contact mode in a mask aligner (Suss

MA 6 Mask Aligner, SUSS MicroTec) with 365 nm light of intensity of 7.5 mW cm^{-2} . The removal of the exposed S1813 photoresist was done by using MF-319 developer (Microchem Inc., USA) for 40 seconds. The Cr/Pt thin film with a thickness of 5/30 nm was deposited by electron beam (e-beam) evaporation onto 4-inch silicon-substrate, while thin Cr film acted as adhesion layer between Pt film and underlying SiN LPCVD film. The deposition rate was kept at 0.1 nm/s during the evaporation process. The Cr/Pt/Photoresist stack were then lifted off in an acetone solution by ultrasonic agitation, leaving desired Cr/Pt pattern on the substrate. Next, the top-side lithography alignment/exposure was employed to pattern SiN beams/pads and a bottom-side lithography alignment/exposure was employed to define etching window for subsequent Si wet etching. These two were conducted under identical condition of the first lithography. Using photoresist pattern as etching mask, the exposed SiN film etching was performed in a commercial reactive ion etcher (Oxford instrument PlasmaPro system 100 RIE). The etching process was carried out in a gas mixture of CHF_3/O_2 with a flow rate ratio of 50/5 sccm, pressure of 55 mTorr, radiofrequency (RF) power of 150 W at room temperature. The SiN etch rate were found to achieve a 49.2 nm min^{-1} . Followed by the SiN etching, the residue photoresist mask was removed with oxygen plasma. At last, wet anisotropic etching of Silicon (Si) was performed by tetramethyl ammonium hydroxide (TMAH) to release the SiN beams/pads.

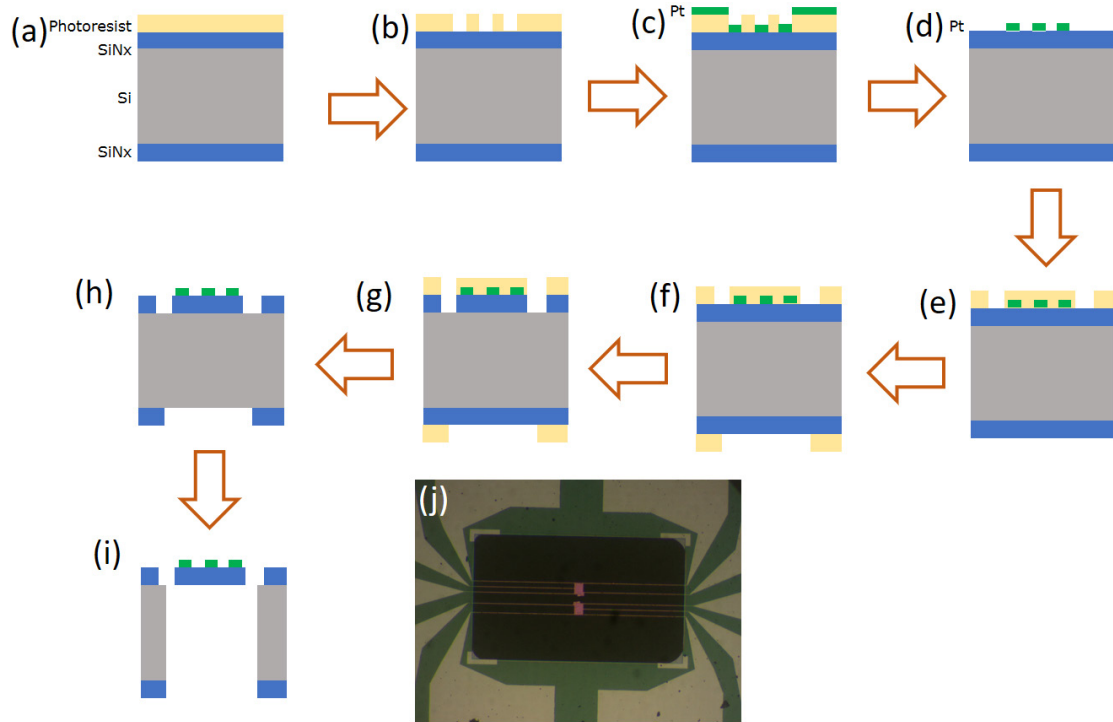


Fig. S2. Schematics of the fabrication process. (a) S1813 was first spin-coated onto the substrate and soft-baked (b) then the PR was exposed and developed. (c) Cr / Pt metal bilayer was deposited using e-

beam evaporation. (d) after the deposition, metal pattern is transfer onto wafer by removing the S1803 and metal stack. (e & f) Defining nitride beam pattern and back open window pattern using standard lithography. (g & h) Pattern transfer process by means of reactive ion etching process with oxford PlasmaPro system 100. (i) Release of suspended SiN pad using tetramethylammonium hydroxide (TMAH) was used to etch the exposed Si region. (j) Optical micrograph of a pair of the as-fabricated device.

S3. A_{th} of SiN_x

Because all the A_{th} 's are normalized to that of a 400 nm thick SiN_x, the A_{th} of the SiN_x is regard as the calibration. Because analytical solutions of many associated quantities can be obtained for thermal conduction in a homogeneous long beam, here, the electron beam is used as a spot heating source focused at the center of a uniform SiN_x beam. Because thermal radiation is negligible, the heat flow thus propagates along the beam to the heat sink at the ends, following a linear temperature distribution. The total absorbed energy (Q) from the e-beam heating can be described as

$$\frac{Q}{K} = \Delta T \quad (S1)$$

where K is the total conductance measured from one end to the other end of the SiN_x beam, and ΔT is the temperature rise at the center of the SiN_x beam. Because ΔT cannot be directed obtained, we instead measure averaged temperature raise $\Delta T_{average}$ by supplying a constant DC current and measuring the Pt film's voltage increase deposited on the SiN_x beam. We then have

$$\frac{Q/2}{2K} = \Delta T = 2\Delta T_{average} \quad (S2)$$

which we can rewrite as

$$Q = 8K\Delta T_{average} \quad (S3)$$

One will obtain the absorbed energy from e-beam heating once the average temperature rise is measured and the conductance is determined by the Joule heating method.

Figure S3(a) shows the SEM image of the beam device, which is made of a suspended 1450 μ m-long and 3 μ m-wide silicon nitride (SiN_x) beam with 30 nm-thick and 2 μ m wide platinum (Pt) film deposited on it. The Pt film's temperature coefficient of resistance is measured in the range of 30-110 $^{\circ}$ C (shown in Fig. S3(b)), in which the temperature is calibrated using a standard PT-1000 thermometer as shown in Figure S3(c).

The thermal conductance of the device at 30-110°C is measured using a self-heating, self-sensing method. A DC electrical current is applied to the device to heat the SiN_x beam, and the corresponding temperature increases $\Delta T_{\text{average}}$ is measured. Under this condition, the temperature rise $\Delta T(x)$ is a parabolic function of the location (x) along the SiN_x beam [5], i.e.

$$\Delta T(x) = -\frac{P}{4\kappa LA}x^2 + C_1x + C_2 \quad (\text{S4})$$

where $P=I^2R$ (R is the total electrical resistance of the Pt film, measured from one end to the other end. The $R(x)$ variation due to temperature distribution is too small and can be ignored here, see below), is the Joule heating power, κ is the effective thermal conductivity, L and A are respectively the half-length and the cross-section area of the SiN_x beam. The constants C_1 and C_2 can be determined by the boundary conditions

$$\Delta T(-L) = \Delta T(L) = 0 \quad (\text{S5})$$

$\Delta T(x)$ and ΔT_{center} are then given by

$$\Delta T(x) = \frac{P}{4\kappa LA}(L^2 - x^2) \quad (\text{S6})$$

and

$$\Delta T_{\text{center}} = \Delta T(0) = \frac{PL}{4\kappa A} \quad (\text{S7})$$

Similarly, our interest is on the relation between Joule heating power and the temperature rise of the whole device ($\Delta T_{\text{average}}$), instead of ΔT_{center} , which cannot be directly measured. Therefore, start with the definition of resistivity

$$dR = \frac{\rho}{A} dx \quad (\text{S8})$$

we have

$$R = \int_{-L}^L \frac{\rho}{A} dx = \frac{1}{A} \int_{-L}^L \rho_0(1 + \alpha\Delta T(x)) dx = \frac{1}{A} \int_{-L}^L \rho_0(1 + \alpha[\frac{P}{4\kappa LA}(L^2 - x^2)]) dx \quad (\text{S9})$$

we can obtain the resistance R as

$$R = R_0[1 + \alpha(\frac{2}{3}\Delta T_{\text{center}})] \quad (\text{S10})$$

Thus the measured $\Delta T_{\text{average}}$ is

$$\Delta T_{\text{average}} = \frac{2}{3}\Delta T_{\text{center}} \quad (\text{S11})$$

We recall

$$\Delta T_{\text{center}} = \Delta T(0) = \frac{PL}{4\kappa A} \quad (\text{S12})$$

Replacing ΔT_{center} by $\Delta T_{\text{average}}$ and rewriting κ to K by the relation $\kappa = K\frac{2L}{A}$, we can

obtain

$$P = 12K\Delta T_{average} \quad (S13)$$

This equation implies that the one-twelfth of the slope of the P vs. $\Delta T_{average}$ graph is the thermal conductance K . Following the above method, we can obtain the thermal conductance of the beam at different temperatures, as presented in Figure S3(d).

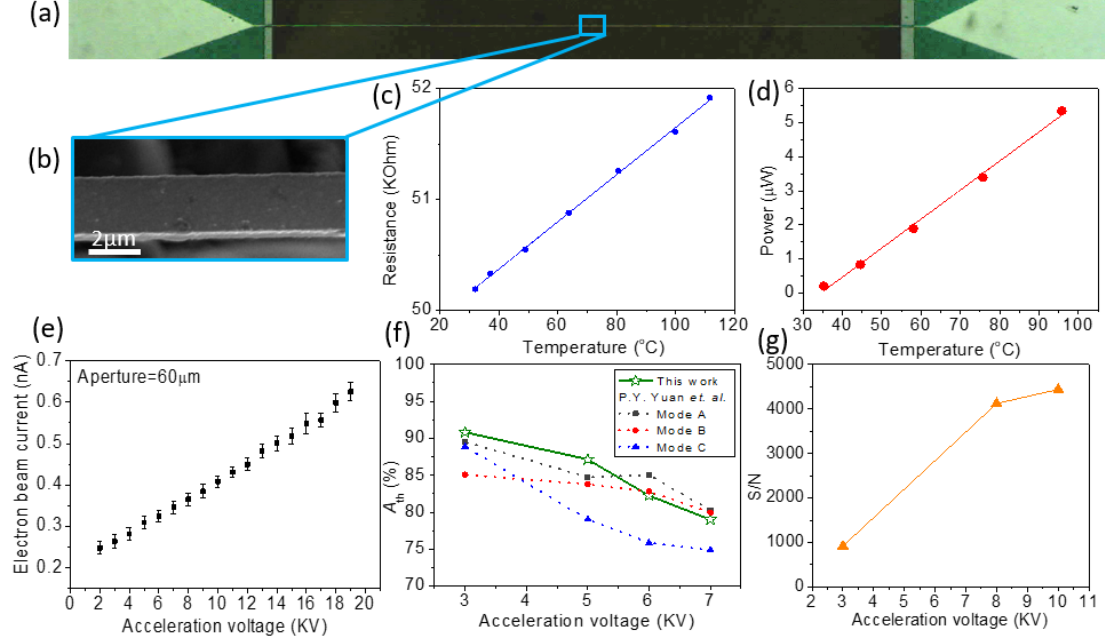


Fig. S3. Device image and characterizations. (a) An optical image of an 1450 μm -long SiN_x beam used for calibrating A_{th} of 400nm thick SiN_x . (b) An enlarged SEM image of the center of the SiN_x beam where the electron beam is positioned. (c) Measured electrical resistance as a function of the temperature of the Pt film deposited on the SiN_x beam. (d) Power vs. temperature raise of the beam when using the self-heating, self-sensing method. From Eq. (S13), the slope of the line represents $1/12^{\text{th}}$ of SiN_x beam's thermal conductance. (e) Electron beam current vs. V_{acc} of our Zeiss Auriga SEM using 60 μm aperture size. (f) Measured A_{th} of the 400nm thick SiN_x vs. V_{acc} . The dotted lines are data from P. Y. Yuan *et al.* (Nano Lett. 2020, 20, (5), 3019-3029), obtained from three current modes. (g) Typical S/N vs V_{acc} when using the spot function of the SEM to heat a sample. The acquisition time is 2 seconds here.

A_{th} can be obtained after normalizing the measured P_{th} by the energy of the incident electron beam, whose current vs. V_{acc} is displayed in Fig. S3(e). Figure S3(f) shows that A_{th} decreases from 91% to 79% when increasing V_{acc} from 3 KV to 7 KV. Similar results from P. Y. Yuan *et al.* (Ref. 9 of the main text) are also shown for comparison. Figure S3(g) shows that S/N generally increases with V_{acc} and can exceed 4000 in our measurements.

S4. Experimental methods on P_{th} mapping

All materials were purchased from Sigma-Aldrich with >95% purity. The SiGe nanowire was grown using chemical vapor deposition method described in Ref. [31]. The samples were either picked up and placed on the platform by a sharpened tungsten tip operated by a piezo-driven manipulator inside a scanning electron microscope (SEM), or dispersed in isopropanol for mild sonication and deposited on the platform.

The SE images were taken by an in-lens SE detector of a Zeiss Auriga SEM. The BSE images were taken by an annular BSE detector located below the objective lens of a JEOL JSM-7800F Prime SEM. As shown in Fig. S4(a), the spot function of Zeiss Auriga SEM, combined with a piezo-driven XY-scanner (SmarAct SLC-1720) controlled by our LabView program, is employed for conducting raster scan to acquire P_{th} mapping. A Keithley 220 current source is used for supplying DC currents and a HP/Agilent 34970A is used to readout the voltage responses from a Wheatstone bridge. Figure S4(b-d) show the experimental raw data when mapping the platform consisting of patterned Pt films deposited on suspended SiN_x under different V_{acc} 's. As shown in Fig. S4(b), we observed that the mapping under $V_{acc}=4$ KV has more dark spots even though both Pt and SiN_x are known to be uniform. Interestingly, the dark spots disappear at higher V_{acc} 's, as shown in Fig. S4(c & d).

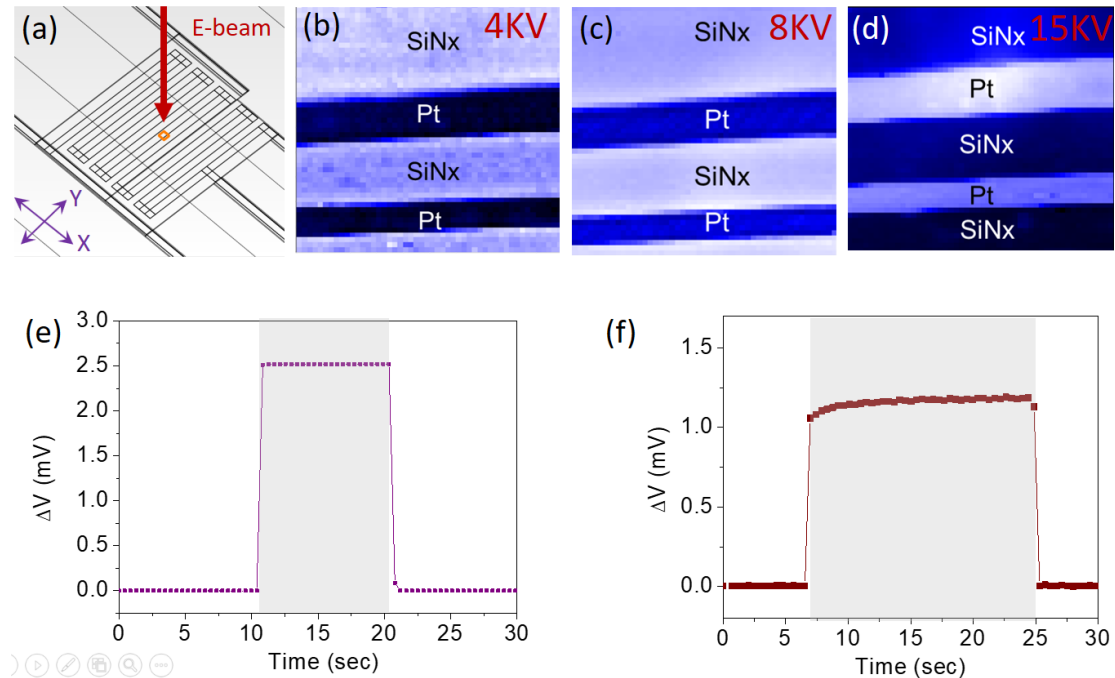


Fig. S4. P_{th} mapping (a) A schematic illustration for conducting P_{th} mapping. The spot function of the SEM is used to position the electron beam at the desired location of the platform to conduct X-Y raster scan. Obtained P_{th} mapping under (b) $V_{acc}=4$ KV, (c) $V_{acc}=8$ KV, and (d) $V_{acc}=15$ KV. Observed voltage responses when the spot of the SEM beam scans from vacuum to a sample (denoted by the shaded area).

Typical voltage response when (e) $V_{acc}>5$ KV and (f) $V_{acc}<5$ KV.

The origin of the dark spots is found to be due to instability of the signal. When $V_{acc}>5$ KV, the typical voltage signal when continuously irradiating a sample using the electron beam is shown in Fig. S4(e), in which the signal quickly stabilizes within 0.45 second. However, we sometimes find that it takes more than 10 seconds before the signal becomes stabilized when $V_{acc}<5$ KV, as shown in Fig. S4(f). The instability of the signal could be attributed to movements or cracking of samples under electron beam irradiation, especially when imaging B or LiH powders. In practice, because each pixel in the P_{th} image usually takes less than 1 sec acquisition time, the presence of the instability would underestimate the signal and make the precise compositional analysis difficult. Empirically, $V_{acc}=5$ KV is chosen and the strongest signals found in the above scans or A_{th} images are selected to plot Fig. 5(b).

S5. Spatial resolution of Z and P_{th}

Here we define the spatial resolution of Z as the minimum distance to correctly identify atomic number of two different materials using our measurement platform. Similar to the knife-edge method of determining resolution in optics, we employ CASINO to simulate A_{th} profile of a SiN_x -Pt edge shown in Fig. S5(a). As shown in Fig. S5(b), the spatial resolution increases from 70nm to 220nm when increasing V_{acc} from 2 KV to 5 KV, but it does not change when increasing the ebeam size from 1nm to 17.5nm. The result suggests that it is the interaction volume rather than the ebeam size that dominates the spatial resolution of Z .

In this work, we do not intentionally pursue high spatial resolution. Thus the SEM imaging condition may not be optimized, and the step and the speed of our piezo-scanner are usually set to acquire a 50 pixels \times 50 pixels P_{th} image within a reasonable time. To evaluate the Z resolution, we select a SiN_x -Pt edge from the upper part of the third image of Fig. 4 (shown in Fig. S5(c), whose color bar has been rescaled to highlight Z variations) as a representative edge profile. As shown in Fig. S5(d), the spatial resolution of Z is estimated to be 250nm. We note that, in practice, the edge profile may be further widened due to the 50nm scanning steps used in our experiments, thus leading to a poorer resolution than obtained from the simulation. The larger A_{th} measured at Pt layer is attributed to the electron penetration into the SiN_x layer at $V_{acc}=5$ KV.

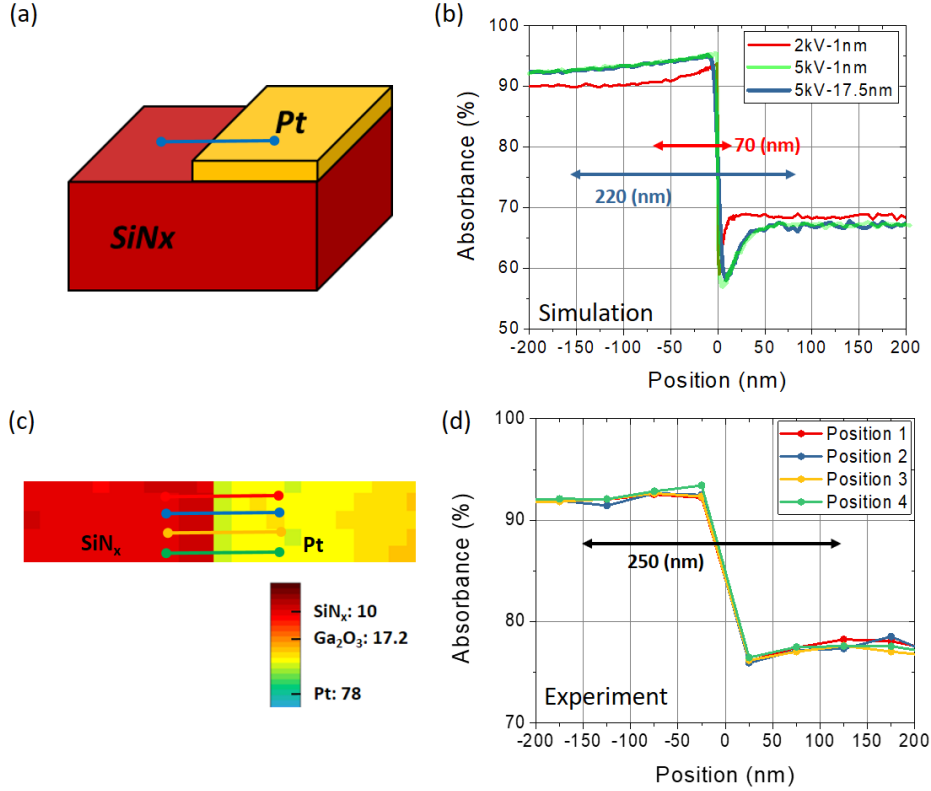


Fig. S5. Spatial resolution of Z at an edge. (a) CASINO simulation of a SiN_x-Pt edge. The thickness of the Pt and SiN_x is 40nm and 500nm, respectively. The blue line denotes the location of the scanned profile. (b) Simulated A_{th} of the edge under different V_{acc} 's (2 KV and 5 KV) and ebeam size (1nm and 17.5nm). The spatial resolution of Z under $V_{acc}=2$ KV and 5 KV are respectively denoted by the red and blue lines. (c) Recolored A_{th} image of a Pt and SiN_x edge (selected from the upper part of the third A_{th} image of Fig. 4) whose color bar has been rescaled to highlight Z variations. (d) A_{th} profile of the edge at different positions. Correct Z identification with the 250nm spatial resolution can be achieved.

In optics, spatial resolution can be also defined as the minimum distance to resolve two separated objects. In our experiment, the case would be more complex in determining the spatial resolution of Z of two objects when their surfaces are not flat. As shown in the inset of Fig. S6(a) where two polygons separated by a 1nm are used to simulate the case of two Ga₂O₃ nanowires in Fig. S6(b). The CASINO simulation shown in Fig. S6(a) suggests that both ebeam sizes and interaction volumes can affect the spatial resolution. Because of the presence of many facets that are not perpendicular to the incident electron beam, the Z identification could be inaccurate. In this regard, what we can test is the image resolution of P_{th} and compare it with that of SEM imaging. Figure S6(b) shows the SEM image of a branched Ga₂O₃ nanowire suspended at the edge of a platform. The corresponding intensity profiles of SE and P_{th} are shown in Fig. S6(c). We see that the profile resembles that of SE and each pixel corresponds to 17.5nm. However, the line profile does not improve much when doubling the pixels,

suggesting that the spatial resolution of P_{th} is 17.5nm and is limited by the electron beam spot size. On the other hand, the spatial resolution of Z is difficult to evaluate here.

The results demonstrate that correct Z mapping with nanoscale resolution can be routinely achieved for flat samples. Further improvements on the spatial resolution of Z may be achieved by lowering V_{acc} and thereby reducing the interaction volume. We note that the same method cannot be applied to EPMA, as it usually requires high voltage and high current operation to acquire sufficiently strong signals. Indeed, low V_{acc} operation and low Z identification are the two major advantages of our technique.

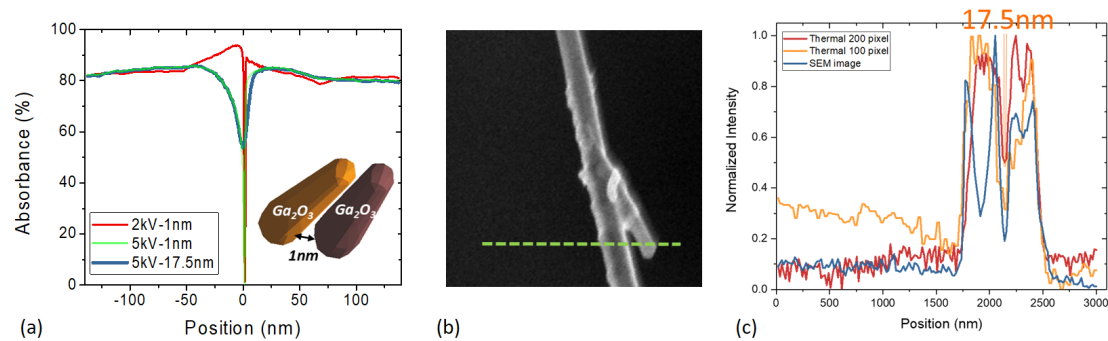


Fig. S6. Spatial resolution of P_{th} . (a) CASINO simulation of the line profile of P_{th} of two polycrystalline Ga_2O_3 nanowires (shown in the inset) under different V_{acc} 's (2 KV and 5 KV) and ebeam sizes (1nm and 17.5nm). (b) SE image of a branched Ga_2O_3 nanowire suspended at the edge of a platform. (c) The intensity profiles of SE and P_{th} for two line scans of different pixels. The line profile is indicated at the dashed line of (b). Each pixel is found to be 17.5nm in the P_{th} scan.

References

- [1] Demers, Hendrix, et al. "Three-dimensional electron microscopy simulation with the CASINO Monte Carlo software." *Scanning* 33.3 (2011): 135-146.
- [2] Browning, R., et al. "Empirical forms for the electron/atom elastic scattering cross sections from 0.1 to 30 keV." *Journal of Applied Physics* 76.4 (1994): 2016-2022.
- [3] Joy, D. C., and Suichu Luo. "An empirical stopping power relationship for low-energy electrons." *Scanning* 11.4 (1989): 176-180.
- [4] Lowney, Jeremiah R. "Monte Carlo simulation of scanning electron microscope signals for lithographic metrology." *Scanning: The Journal of Scanning Microscopies* 18.4 (1996): 301-306.
- [5] T. L. Bergman, A. S. Lavine, and F. P. Incropera. *Fundamentals of Heat and Mass Transfer*. 7th edn, (Wiley, 2011).